

Modeling Flowslides Caused by Static Loading

R. PHILLIPS AND P. M. BYRNE

The phenomenon of liquefaction can occur in saturated loose sands and is characterized by a large strength or stiffness loss resulting in substantial deformation or a flowslide when subjected to rapid static or cyclic loading. To study this phenomenon, the Canadian geotechnical engineering community has started the Canadian Liquefaction Experiment (CANLEX), which has planned to include a large, controlled liquefaction event in the field. Numerical predictions of the response of this full-scale event will be compared with the field measurements. Centrifuge model tests are being conducted to aid in the design of the field event and to allow for calibration of the numerical models. These tests could serve as a substitute for calibration of numerical models in the event that a dynamic field event is not possible or not conducted at the site. The first of these tests ascertained that a gravitational flowslide event could be induced under undrained static loading. A surcharge dropped on the crest of an equivalent 16-degree submerged 8.8-m-high slope of loose oil sand tailings caused the slope to liquefy and flow with deep-seated lateral movements throughout the soil slope to an angle of 7 degrees. A finite difference numerical model, calibrated against laboratory element test data, captured the essence of the observed undrained response of the centrifuge test in terms of pore pressure rise and deformation pattern. These modeling techniques will be used to evaluate other triggering mechanisms for the field event.

The Canadian geotechnical engineering community has started a major \$1.8 million (Canadian) sand liquefaction study entitled the Canadian Liquefaction Experiment (CANLEX) through the collaborative efforts of industry, engineering consultants, and university participants, and with support from the Natural Sciences and Engineering Research Council of Canada (NSERC). The study will examine the characterization of sand for dynamic and static liquefaction. The phenomenon of liquefaction occurs in saturated loose sands and is characterized by a large strength loss resulting in substantial deformation when the sand is subjected to rapid static or cyclic loading. The objectives of sand characterization are as follows (1):

1. To obtain high-quality undisturbed samples through in situ freezing techniques.
2. To calibrate and verify in situ testing techniques including those under the influence of high overburden stress.
3. To obtain greater understanding of the mechanism of liquefaction-induced displacement through the development and evaluation of analytical models.
4. To investigate other factors such as influence on liquefaction of fines content, fabric, direction of loading, shape of state boundaries, and triggering mechanisms.

R. Phillips, C-CORE, Memorial University of Newfoundland, St. John's, Newfoundland, A1B 3X5 Canada. P. M. Byrne, Department of Civil Engineering, University of British Columbia, Vancouver, British Columbia, V6T 1W5 Canada.

CANLEX comprises three phases over 3 years. Phases 1 and 2 are concerned with characterization of loose sand to determine its in situ state and elemental stress-strain response. These phases will involve both in situ tests and recovery of high-quality samples for laboratory testing. The purpose of such characterization is to understand further the liquefaction phenomenon and to specifically evaluate triggering resistance, residual strength, and liquefaction-induced displacement of embankments and slopes under static and earthquake loading conditions. The Phase 1 field characterization of hydraulically deposited sand at the Syncrude Canada Limited Mildred Lake Settling Basin, Fort McMurray, Alberta, has been successfully completed. Phase 2 has commenced with test sites in the Fraser River Delta in Richmond, British Columbia (2).

In Phase 3, a controlled liquefaction event will be initiated at the Syncrude tailings disposal site and will involve construction of a loose sand berm and the triggering of a static flow liquefaction event. Numerical modelers will predict the response of this full-scale event and compare the numerical response with the field measurements.

In the project entitled Verification of Liquefaction Analysis Using Centrifuge Studies, the relevance and effectiveness of existing numerical and constitutive models used in the analysis of soil liquefaction were also evaluated (3). It was concluded that centrifuge modeling was a reliable tool for studying the mechanisms of soil behavior in such boundary-valued problems and that fully coupled effective stress-based numerical procedures using plasticity-based constitutive models were most promising for the prediction of deformation.

The CANLEX project includes centrifuge testing of reduced-scale physical models of potential full-scale events. The objectives of these tests have been described. In Stage 1 of these tests, described by Phillips and Byrne (4), the feasibility of modeling static liquefaction in the centrifuge was ascertained. Subjecting a submerged loose sand slope to a crest loading applied at an appropriate rate brought about an undrained flowslide. In this paper the characteristics of this flowslide are compared with a Class B prediction from a numerical model.

MATERIAL PROPERTIES

Laboratory Measurements

The sand used was moist oil sand tailings supplied by Syncrude Canada Limited. Table 1 presents properties of this fine subangular to subrounded sand determined in accordance with ASTM Schedule D procedures, except the trace oil content. The grain size distribution is shown in Figure 1. The response of undrained triaxial extension and compression tests and drained compression tests are

TABLE 1 Properties of Oil Sand Tailings

Specific gravity, G_s		2.64
Maximum void ratio, e_{\max}		0.96
Minimum void ratio, e_{\min}		0.53
Mean grain size, d_{50}	mm	0.17
Effective grain size, d_{10}	mm	0.092
Uniformity coefficient, C_u		2.12
Natural water content, w	%	7 - 9
Oil content	%	0.27
Permeability to Canola oil @ 21°C	m/s	3.3e-07
at relative density, D_r		0.40
Permeability to water @ 21°C	m/s	1.6e-05
at relative density, D_r		0.48

summarized in Figure 2. The samples tested were of water-saturated oil sand with an average relative density of 40 percent. These were tested at an axial strain rate of about 2 percent/min. The normal and deviator stresses s' and t in Figure 2(b) are $(\sigma'_1 + \sigma'_3)/2$, and $(\sigma'_1 - \sigma'_3)/2$, respectively. The projection of the critical state or constant volume line in stress space has a friction angle, $\phi \leq \phi_{cv}$, of about 36 degrees. The instability line in triaxial extension, taken as the locus of maximum deviator stress, has a mobilized friction angle of 13 degrees.

Typical stress-strain responses from both undrained triaxial compression and extension tests are shown in Figure 2(a). In compression, the material is strain hardening, and such a material would not be expected to undergo static liquefaction. In extension, however, a strain-softening liquefaction response is noted, and such a material could undergo static liquefaction.

CENTRIFUGE MODELING

Centrifuge modeling is a technique for reduced-scale physical modeling of gravity-dependent phenomena, such as soil slope behavior. Because a full-scale soil structure is in equilibrium under the Earth's

gravitational field, g , a reduced-scale model on a centrifuge, at radius R , is in equilibrium under an acceleration field of $R\omega^2$, where ω is the rotational speed. The model will then have its weight increased N times, where $N = R\omega^2/g$.

For a typical value of $N = 100$, if a model is made at 1/100th scale and is accelerated to 100g, the stresses caused by self weight will be similar to the stresses in the prototype at homologous points. The model can then reproduce the phenomena of cracking, rupture, or flow that would be observed in the prototype because the stress dependency of soil behavior has been correctly simulated. The principles, scaling laws, and some applications of centrifuge modeling are described by Schofield (5) and Leung et al. (6).

Centrifuge Model Test

The centrifuge model test comprised an instrumented plane-strain submerged loose sand with 16-degree slope at a relative density of about 30 percent, as shown in Figure 3. The test was conducted at 50g for a scaled slope height of 8.75 m. Two pore pressure transducers (PPT 1 and PPT 2) were placed within the sand model under the center of the crest and at the midpoint of the slope, respectively, as shown. The model tests were conducted at the C-CORE Centrifuge Centre, St. John's, Newfoundland (7).

The sand slope was saturated with a viscous pore fluid, namely, Canola vegetable oil with a dynamic viscosity of 57 centipoise at 21°C. Comparison of both water-saturated and oil-saturated drained triaxial tests confirmed that the oil did not affect the skeletal response of the sand. For water-saturated sand, the coefficient of consolidation, c_v , at 50 kPa is about 200 cm²/sec, which is possibly too large to control the escape of water and cause a liquefaction event in the centrifuge test. The more viscous pore fluid retards pore pressure dissipation, permitting liquefaction to develop. The oil viscosity is approximately 50 times that of water, which will reduce c_v by a factor of 50. The use of such a viscous pore fluid ensures synchronous time scaling of inertial and consolidation events (8).

Preliminary analyses indicated that even with oil rather than water as a pore fluid, the crest load would have to be applied in a few seconds to prevent significant dissipation of pore pressures. Such dissipation would prevent the triggering of static liquefaction. For this reason, a drop weight approach was used. The weight was composed of a steel surcharge suspended above the slope crest. The sand slope was subjected to Loading Sequences A and B, as described in the next two sections.

Loading Sequence A

For Sequence A, the surcharge had a static bearing pressure of 43 kPa and was suspended 11 mm above the initial slope crest. The slope crest settled 6 mm during acceleration of the centrifuge to 50g at middepth of the sand slope. The surcharge struck the sand surface with a velocity of more than 0.6 m/sec. Both PPTs recorded an instant increase of about 32 kPa, which is 74 percent of the static bearing pressure (Figure 4). The pore pressure at PPT 1 continued to increase by 8 kPa for another 2.5 sec because of pore pressure redistribution under the impermeable surcharge. No significant movements of the sand slope were observed by a video monitoring system. This observation was confirmed by the PPTs as the pore pressures eventually dissipated to their initial equilibrium values.

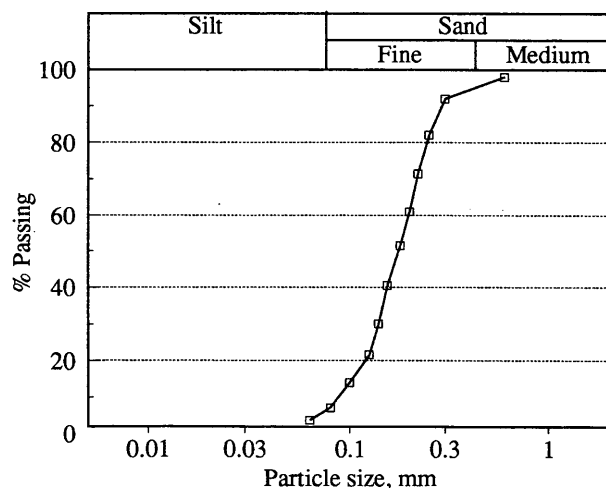


FIGURE 1 Oil sand particle size distribution.

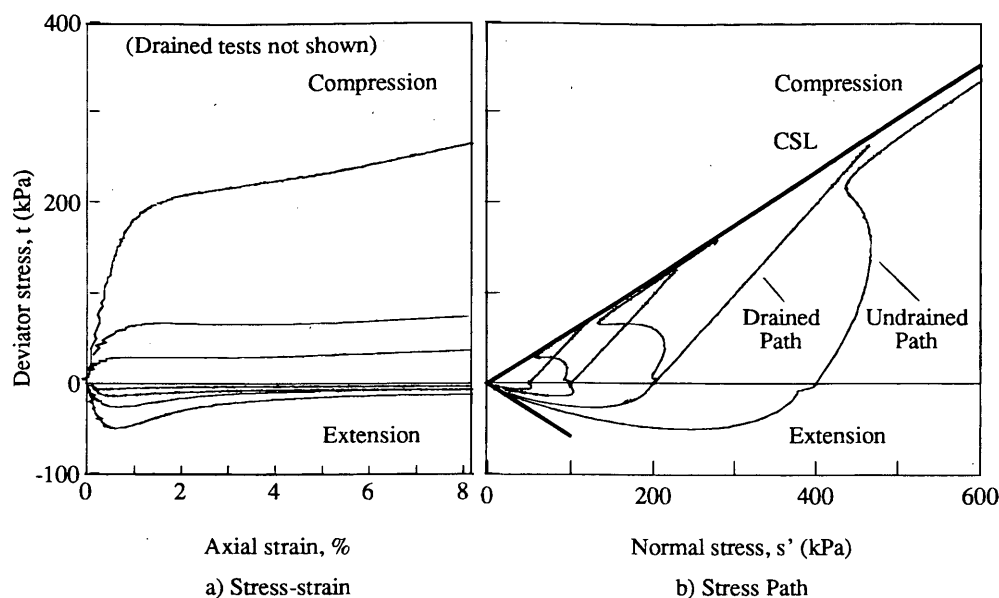


FIGURE 2 Oil sand triaxial response.

Loading Sequence B

The centrifuge was stopped and the surcharge increased to a static bearing pressure of 87 kPa suspended 18 mm above the compressed slope crest. The centrifuge was accelerated again to 50g and the surcharge dropped. The actual drop height exceeded 21 mm because of embedment of the surcharge into the crest of the slope. The measured impact velocity exceeded 0.1 m/sec and probably exceeded 0.6 m/sec, as measured in Loading Sequence A. The 42-kPa step rise at PPT 1 was 48 percent of the surcharge static bearing pressure (Figure 5). The continued rise at PPT 1 of 27 kPa for 4 sec after impact is partly because of downward movement of PPT 1 during embedment of the surcharge. The initial total stress above PPT 2 was about 106 kPa. The pore pressure at PPT 2 rose to 90 percent of this value, indicating the potential for liquefaction adjacent to this transducer.

The video record matches the events recorded by PPT 1. After dropping of the weight, no gross distortion of the slope was observed for a short period of about 1/4 sec. The surcharge then

punched vertically down into the crest of the slope and large deep-seated lateral soil flow movements were observed throughout the soil slope toward the slope toe. These movements stopped after a 3-sec period. A shear plane developed vertically down from the edge of the drop weight adjacent to the shoulder of the slope. The final slope profile with the positions of the surcharge and the PPTs is shown in Figure 6. The slope came to rest at an angle of about 7 degrees. The lateral slope movement was constrained by the end wall of the test section.

NUMERICAL MODELING

The numerical simulation of the centrifuge test uses a finite difference solution of the governing equations incorporating an elastic-plastic stress-strain model that captures the fundamental drained or skeleton behavior of sand. The undrained behavior is predicted by imposing the volumetric constraint that arises from the presence of the water. Details of the stress-strain law used in the analysis are

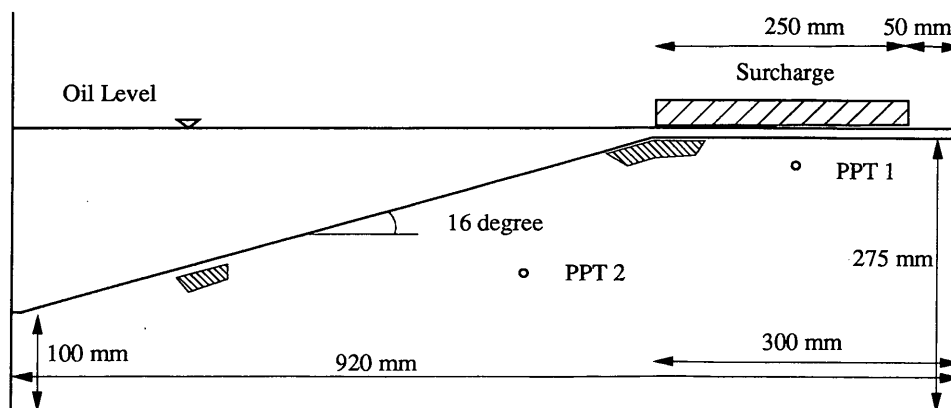


FIGURE 3 Centrifuge test geometry.

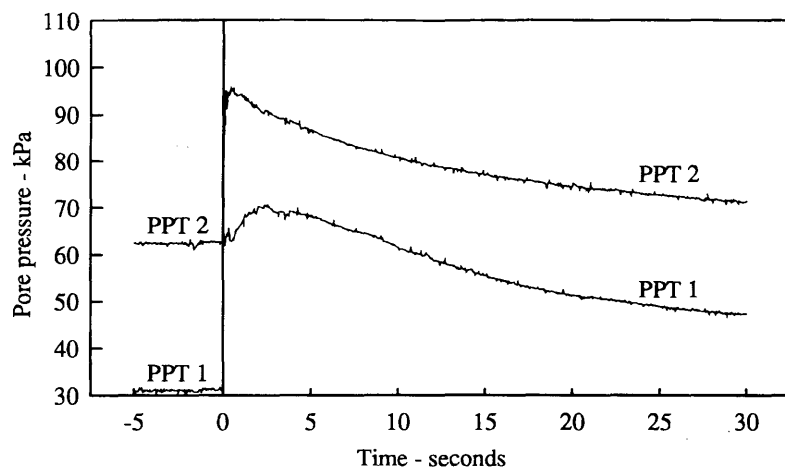


FIGURE 4 Pore pressure response to loading sequence A.

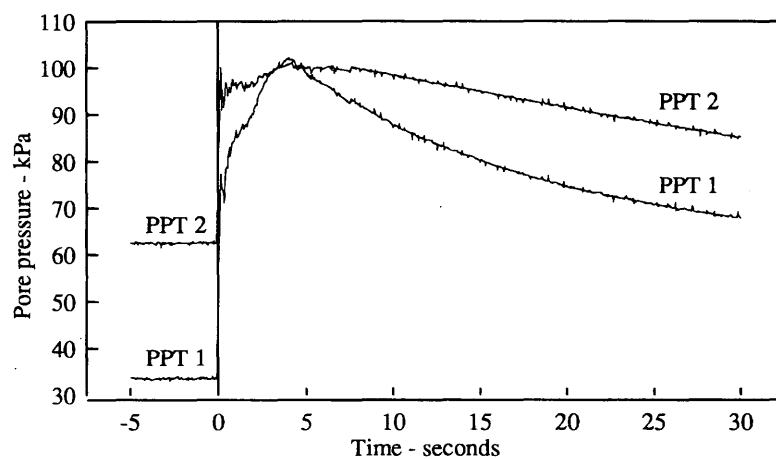


FIGURE 5 Pore pressure response to loading sequence B.

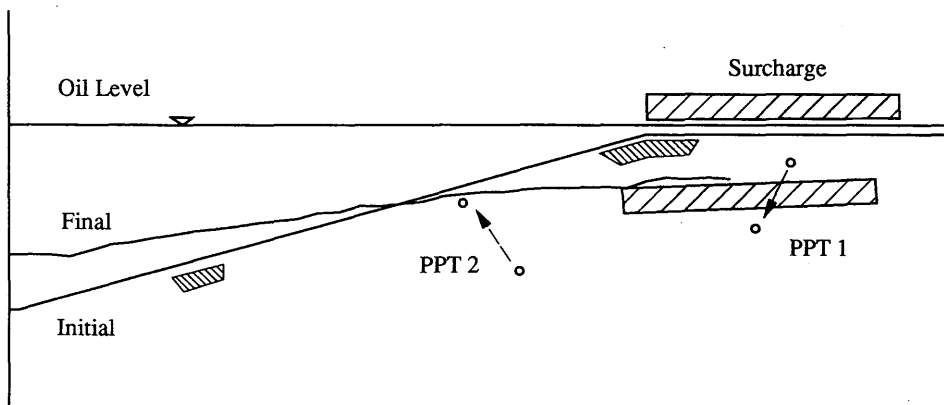


FIGURE 6 Initial and final slope configurations.

presented in the following section. The numerical model is first used to capture the laboratory stress-strain response of test elements and then applied to predict the response of the centrifuge model.

Stress-Strain Model

Both the drained and the undrained responses of granular material are controlled by the skeleton behavior. The effective stress ratio t/s' and the density basically control the shear response as shown in Figure 7(a). Shear strains induce volumetric strains as shown in Figure 7(b). Basically, loose material is contractive when sheared to any effective stress ratio state, whereas dense material is contractive for stress ratio states below the phase transformation or constant volume friction angle and dilative for stress ratio states above [Figure 7(d)]. At very low confining stress, loose material may behave as a dense material and may be dilative at large strains. Unloading and reloading during shear (not shown) would promote a stiff, essentially elastic response. Thus the major portion of the observed strain during first loading is plastic rather than elastic, and these plastic strains dominate the response. The elastic-plastic stress-strain model used to capture such behavior is discussed in the following section.

Elastic Properties

The elastic properties are assumed to be isotropic and defined by two stress-level-dependent elastic parameters, a shear modulus G_e and bulk modulus B_e as follows:

$$G_e = K_{ge} \cdot P_a \cdot (s'/P_a)^{ne} \quad (1)$$

where

K_{ge} = the shear modulus number,
 ne = shear modulus exponent, and
 P_a = atmospheric pressure in the units selected.

$$B_e = K_{be} \cdot P_a \cdot (s'/P_a)^{me} \quad (2)$$

where K_{be} is the bulk modulus number, and me is the bulk modulus exponent.

The values of the parameters K_{ge} , K_{be} , ne , me can be obtained from unloading tests. In the absence of such data for the Syncrude sand, values of $K_{ge} = 300$, $K_{be} = 300$, $ne = 0.5$, and $me = 0.5$ were selected. The bulk modulus parameters K_{be} and me were based on isotropic drained unloading tests on other loose granular material. The shear exponent parameter ne was set to 0.5. The shear modulus number K_{ge} was set equal to K_{be} to conform with that of Hardin (9), who determined Poisson's ratio for sand to be in the range 0 to 0.2 and recommended a value of about 0.12. The increments of elastic strain for any stress increment are determined from these two stress-level-dependent elastic moduli, G_e and B_e .

Plastic Properties

The variation of deviator stress ratio η (t/s') with plastic shear strain [Figure 7(a)] is assumed to be hyperbolic. The slope of this line is the normalized plastic tangent modulus $G_p^* = G_p/s'$, where the tangent plastic shear modulus G_p is given by

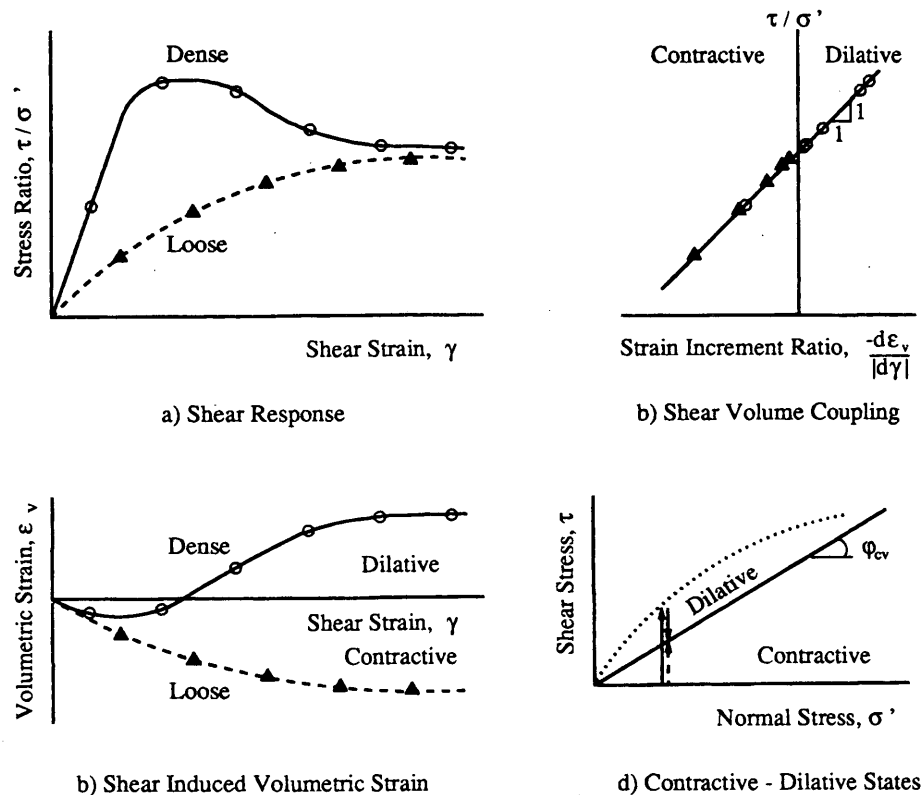


FIGURE 7 Response of granular skeleton to monotonic shear loading.

$$G_p = K_{gp} \cdot P_a \cdot (s'/P_a)^{np} (1 - t/t_f \cdot R_f)^2 \quad (3)$$

where

- K_{gp} = plastic shear modulus number,
- np = plastic shear modulus exponent,
- t_f = shear strength = $s' \sin(\varphi)$
- R_f = failure ratio, t_{ult}/t_f , generally in the range of 0.5 to 1.0, and
- t_{ult} = ultimate stress from the best-fit hyperbola.

This approach is similar to that of Duncan and Chang (10) except that solely plastic strains, rather than the combination of elastic and plastic strains, are considered. An increment of plastic shear strain, $d\epsilon_y^p$, is caused by an increase in stress ratio, $d\eta$, where

$$d\epsilon_y^p = d\eta/G_p^* = d\eta/(G_p/s') \quad (4)$$

since $\eta = t/s'$

$$d\eta = dt/s' - tds'/s'^2 \quad (5)$$

Hence,

$$d\epsilon_y^p = \frac{1}{G_p} \left[dt - \frac{t}{s'} ds' \right] \quad (6)$$

An increase in stress ratio can be brought about by an increase in shear stress or a decrease in normal effective stress. Either change will cause an increment of plastic shear strain, $d\epsilon_y^p$, as may be seen from Equation 6. If $ds' = 0$, as it would be for a drained simple shear test, then the usual definition of G_p is obtained. If $dt = 0$, then a reduction in effective stress ($-ds'$) will still cause a plastic shear strain increment $d\epsilon_y^p$ as shown in Figure 8. For undrained tests in which a significant pore water pressure rise occurs, ds' will be negative and lead to a significant increase in plastic shear strain. Positive values of ds' are neglected in Equation 6 because they cause a reduction in stress ratio, which causes an elastic (not plastic) strain. The second term inside the bracket of Equation 6 is a key feature of the model and is not generally considered in stress-strain modeling of sand. Equation 6 gives the plastic shear strains. To complete the picture, the associated plastic volume changes are also needed.

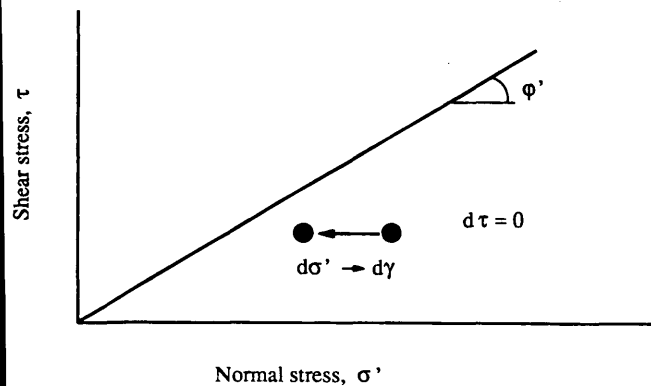


FIGURE 8 Strain increment because of reduction in normal effective stress.

The increment of plastic volumetric strain $d\epsilon_v^p$ is related to the increment of plastic shear strain and is obtained from energy considerations following the concepts of Taylor (11), Schofield and Wroth (12), and Matsuoka and Nakai (13) that the plastic work increment is dissipated solely in friction against the plastic shear strain increment:

$$d\epsilon_v^p = d\epsilon_y^p (\sin\varphi_{cv} - t/s') = d\epsilon_y^p \cdot Dt \quad (7)$$

where

- $d\epsilon_v^p$ = plastic volumetric strain increment
- φ_{cv} = constant volume friction angle, and
- t/s' = deviator stress ratio on the plane of maximum shear stress, taken here to be the mobilized plane.

The term $D_t (\sin\varphi_{cv} - t/s')$ controls the shear-induced volumetric contraction or dilation. Contraction occurs for stress ratios less than $\sin\varphi_{cv}$ and dilation for stress ratios greater than $\sin\varphi_{cv}$. Because planes of principal stress and strain increment are assumed to coincide, the normal plastic strain $d\epsilon_n^p$ on the mobilized plane is half the plastic volumetric strain $d\epsilon_v^p$. Hence, from Equations 6 and 7 the plastic stress-strain relationship on the mobilized plane is

$$\begin{Bmatrix} d\epsilon_n^p \\ d\epsilon_y^p \end{Bmatrix} = \frac{1}{G_p} \begin{bmatrix} -t/s' \cdot D_t/2 & D_t/2 \\ -t/s' & 1 \end{bmatrix} \begin{Bmatrix} ds' \\ dt \end{Bmatrix} \quad (8)$$

In general, the direction of the mobilized plane does not correspond with the reference coordinate system, and the stress-strain response is transformed into the following form:

$$\begin{Bmatrix} d\epsilon_x^p \\ d\epsilon_y^p \\ d\gamma_{xy}^p \end{Bmatrix} = [C_p] \begin{Bmatrix} d\sigma_x' \\ d\sigma_y' \\ d\tau_{xy} \end{Bmatrix} \quad (9)$$

in which C_p is the plastic strain matrix linking the x, y Cartesian coordinates of the stress and plastic strain increment vector. The elastic and plastic strains are then added, and the matrix is inverted to give the stress increments in terms of the strain increments.

$$\{\Delta\sigma'\} = \begin{Bmatrix} d\sigma_x' \\ d\sigma_y' \\ d\tau_{xy} \end{Bmatrix} = [D_{ep}] \begin{Bmatrix} d\epsilon_x \\ d\epsilon_y \\ d\gamma_{xy} \end{Bmatrix} = [D_{ep}] \{d\epsilon\} \quad (10)$$

Coaxiality of the plastic strain increments and the associated principal stresses is assumed in performing this transformation. The effective stress-strain response of the soil skeleton to loading under drained conditions is thus described in Equation 10. In classical plasticity terms, the yield loci comprise lines of constant stress ratio with a nonassociated flow rule given by Equation 8 and a hardening law defined in terms of plastic shear strain in Equation 6.

Undrained Response

For undrained conditions the increment of pore fluid pressure, du , is given by

$$du = B_f/n \cdot d\epsilon_v^f \quad (11)$$

where

B_f = bulk modulus of the pore fluid,
 n = porosity of the skeleton, and
 $d\epsilon_v^f$ = volumetric strain of the fluid expressed in terms of the total volume of the element.

For undrained conditions, volume compatibility requires that the volumetric strain of the soil skeleton, $d\epsilon_v$, must equal the volumetric strain of the fluid, $d\epsilon_v^f$, thus

$$d\epsilon_v^f = d\epsilon_v = d\epsilon_x + d\epsilon_y = \begin{Bmatrix} 1 \\ 1 \\ 0 \end{Bmatrix}^T \begin{Bmatrix} d\epsilon_x \\ d\epsilon_y \\ d\gamma_{xy} \end{Bmatrix} \quad (12)$$

Hence

$$du = \frac{B_f}{n} = \begin{Bmatrix} 1 \\ 1 \\ 0 \end{Bmatrix}^T \begin{Bmatrix} d\epsilon_x \\ d\epsilon_y \\ d\gamma_{xy} \end{Bmatrix} \quad (13)$$

and

$$\{du\} = \begin{Bmatrix} du \\ du \\ 0 \end{Bmatrix} = \frac{B_f}{n} \begin{Bmatrix} 1 \\ 1 \\ 0 \end{Bmatrix} \begin{Bmatrix} 1 \\ 1 \\ 0 \end{Bmatrix} \{d\epsilon\} = \frac{B_f}{n} \begin{bmatrix} 1 & 1 & 0 \\ 1 & 1 & 0 \\ 0 & 0 & 0 \end{bmatrix} \{d\epsilon\} = [D_f] \{d\epsilon\} \quad (14)$$

now

$$d\sigma = d\sigma' + du \quad (15)$$

Hence

$$\{d\sigma\} = \{d\sigma'\} + \{du\} = [[D_{ep}] + [D_f]] \{d\epsilon\} \quad (16)$$

The stress-strain model for the special case of undrained conditions is thus obtained in terms of total stresses by adding the effective and

pore fluid contributions to stiffness. At each step of the analysis, the change of pore fluid pressure is obtained from the computed element strains using Equation 11. The stress-strain model is therefore a fully coupled effective stress model.

Numerical Analysis Procedure

In general, stress-deformation response is governed by the laws of mechanics, which require that equilibrium and compatibility be satisfied for the given boundary conditions and the appropriate stress-strain law. Finite element or finite difference techniques are routinely used to reasonably satisfy these conditions.

The analysis was carried out using the computer code Fast Lagrangian Analysis of Continua (FLAC), Version 3.2 (14). This program uses a finite difference technique. The domain is discretized into a quadrilateral grid in which each grid zone or element comprises four triangles. The stiffness contribution of each zone is essentially the same as if it were represented by four constant strain finite elements. Dynamic equilibrium, rather than static equilibrium, is satisfied using a step-by-step explicit time domain procedure. Large strains and displacements are approximated by upgrading the nodal coordinates.

This approach has the advantage that the solution is numerically stable even when the problem is not statically stable. In this way, development of large strains and displacements before failure can be examined. The code allows the user to input the specific stress-strain model. The modified Matsuoka model [after Matsuoka and Nakai (13)] discussed in the previous section was used for the analyses described hereafter.

Numerical Simulation of Triaxial Tests

The undrained response observed in the triaxial tests was first captured using the FLAC code and the stress-strain model described previously. The predicted and observed responses for undrained triaxial compression and extension tests for a confining stress of 100 kPa are compared in Figure 9. The predicted undrained triaxial compression response [Figure 9(a)] is strain-hardening, whereas the

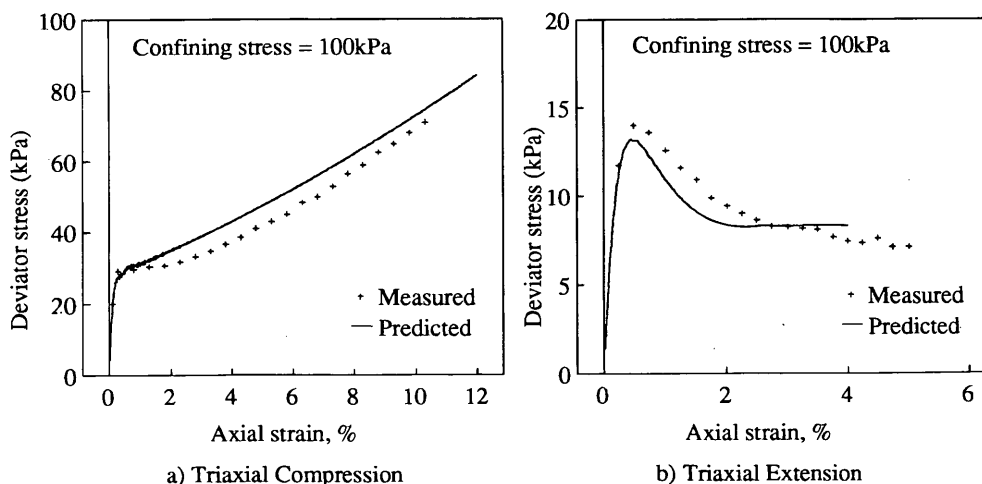


FIGURE 9 Comparison of oil sand undrained response.

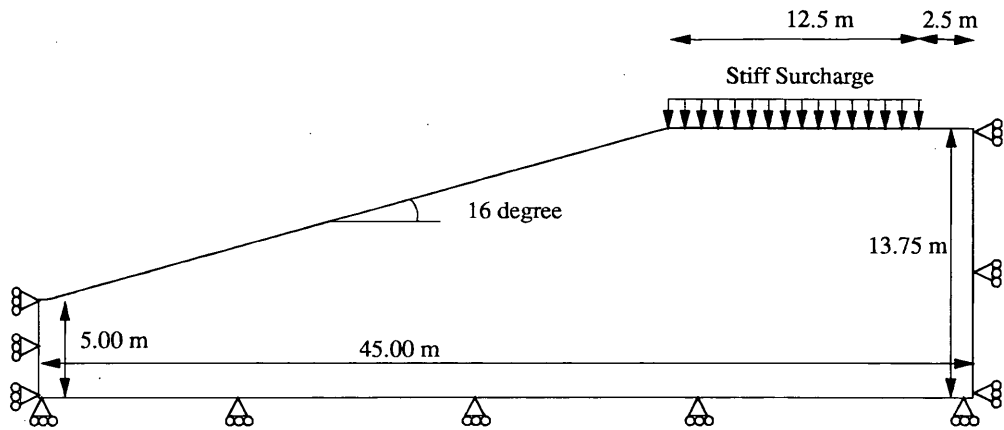


FIGURE 10 Slope geometry and boundary conditions simulated in numerical model.

extension response [Figure 9(b)] is strain-softening. This stress path dependency or anisotropy is captured in the modeling procedure by making the plastic shear modulus a function of the direction of the major principal compressive stress, σ'_1 . The model parameters were selected to provide the best fit to the observed data. The elastic parameters used were stated previously.

The plastic parameters used to capture the undrained extension (σ'_1 horizontal) behavior were $K_{gp} = 100$, $np = 0.5$, $R_f = 0.95$, $\epsilon = 30$ degrees, $\phi_{cv} = 30$ degrees. The stiffer response in vertical compression (σ'_1 vertical) was captured using a stiffer $K_{gp} = 300$ and $\phi = 31$ degrees. Because $\phi > \phi_{cv}$, this will cause dilation and strain hardening at large strains.

In the centrifuge analysis, the stress path followed will range from vertical compression beneath the applied load to vertical extension (horizontal compression) in the toe area. To allow for this stress rotation, it was assumed that $K_{gp} = 100$ and $\phi = 30$ degrees for $0 < \alpha < 45$ degrees, $K_{gp} = 100 (1 - 2 \cos 2\alpha)$ and $\phi = (30 - \cos 2\alpha)$ degrees for $45 < \alpha < 90$ degrees, where α is the angle between the direction of major principal stress and the horizontal axis. Thus for $0 < \alpha < 45$ degrees representing horizontal compression through simple shear conditions K_{gp} and ϕ are constant. For $45 < \alpha < 90$ degrees representing simple shear to vertical compression there is a continuous increase in K_{gp} and ϵ from 100 to 400 and 30 to 31 degrees, respectively. The numerical model is used in the following section with these calibrated parameters to predict the response of the centrifuge model test.

Numerical Simulation of Centrifuge Test

The scaled model or prototype having the dimensions shown in Figure 10 was used for analysis purposes. The discretized grid or element mesh is shown in Figure 11. The effective stresses in the model before the application of the loads were computed using a submerged unit weight of 9.0 kN/m³ and a drained analysis.

The responses to Loading Sequences A and B were obtained by applying pressures of 43 and 87 kPa, respectively, at the surface. The inertia effect of dropping the weight was not completely simulated. However, because FLAC uses a dynamic solution technique, inertia effects corresponding to the sudden application of load under zero drop are simulated.

The predicted and observed excess pore pressures at PPT 1 and

2 for the two loading sequences are compared in Table 2. The predicted pore pressures at PPT 1 are in reasonable agreement with those observed for both load cases. The predicted pore pressures at PPT 2 are lower than those observed. This may be because of the impact loading, which was not completely simulated in the analysis. Contours of excess pore pressure are shown in Figure 12.

The predicted deformations for Loading Sequence A were small and are not shown. The predicted displacements for Loading Sequence B (Figure 13) show a deep-seated pattern of movements, which is in general agreement with the observed pattern. The predicted movements are slightly smaller than those observed, which may be because of the effect of impact loading, which was not completely simulated in the analysis.

CONCLUSIONS

In Stage 1 of the CANLEX centrifuge testing, conducted on the C-CORE centrifuge, it was determined that a static liquefaction

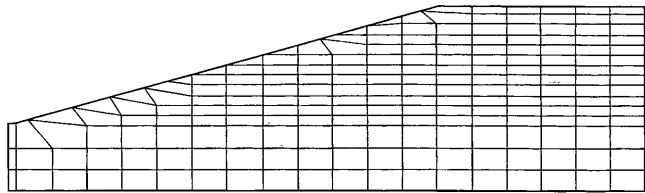
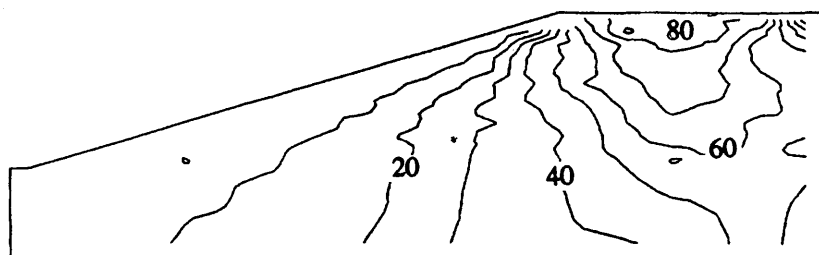


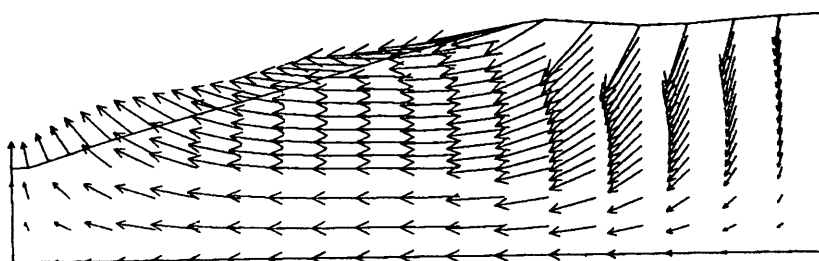
FIGURE 11 Finite difference mesh.

TABLE 2 Comparison of Excess Pore Pressures after Surcharging				
(kPa)	Load case A		Load case B	
	Measured	Predicted	Measured	Predicted
PPT1	38	36	68	70
PPT2	32	14	42	28



Contours at 10 kPa intervals from 0 to 90 kPa.
Contour for 0 kPa is on left hand side.

FIGURE 12 Contours of excess pore pressure, load case B.



Displacement vector magnification factor: 4.6.

FIGURE 13 Displacement vectors, load case B.

event could be induced in a centrifuge test. The centrifuge test involved construction of a 16 degrees submerged slope of oil sand tailings at a relative density of about 30 percent. During the centrifuge test, the prototype slope height was equivalent to 8.8 m. A steel surcharge dropped on the slope crest caused the slope to liquefy and flow to an angle of 7 degrees. Stage 2 of the centrifuge testing will simulate more closely the proposed field event, for which a number of triggering mechanisms are under consideration.

The numerical model presented enables us to capture static liquefaction behavior in loose sand. The numerical modeling was based on the initial capturing of the observed element behavior in both triaxial compression and extension. This behavior was used to predict the centrifuge tests. The predicted pore pressures at PPT 1 under the load were in good agreement with those measured, whereas the prediction of PPT 2 was too low. The pattern and magnitude of predicted displacements were in general agreement with those observed. The larger pore pressures measured may have been because of the impact loading, which was not simulated in the numerical analysis.

ACKNOWLEDGMENTS

The authors acknowledge the support provided through the CANLEX project from a NSERC Collaborative Research and Development Grant. C-CORE's provision of centrifuge facilities and technical assistance is also acknowledged. The authors are

grateful to Yi Ning Zeng of the University of British Columbia for her assistance with the numerical analysis.

REFERENCES

1. CANLEX. *CANLEX Newsletter*, Vol. 1, No. 1, June 1993.
2. CANLEX. *CANLEX Newsletter*, Vol. 2, No. 1, June 1994.
3. Arulanandan, K., and R. F. Scott. *Verification of Numerical Procedures for the Analysis of Soil Liquefaction Problems*, Vol. 2. A. A. Balkema, Rotterdam, The Netherlands, 1994.
4. Phillips, R., and P. M. Byrne. Modelling Slope Liquefaction Due to Static Loading. Preprints of 47th Canadian Geotechnical Conference, Halifax, Nova Scotia, Canada, September 1994.
5. Schofield, A. N. Cambridge Geotechnical Centrifuge Operations. Twentieth Rankine Lecture. *Geotechnique*, Vol. 30, No. 3, 1980, pp. 227-268.
6. Leung, C. F., F. H. Lee, and T. S. Tan. Centrifuge 94. *Proc., International Conference on Geotechnical Centrifuge Modelling*, Singapore, A.A. Balkema, Rotterdam, The Netherlands, September 1994.
7. Phillips, R., J. I. Clark, M. J. Paulin, R. Meaney, D. E. L. Millan, and K. Tuff. Canadian National Centrifuge Centre with Cold Regions Capabilities. *Proc., International Conference on Geotechnical Centrifuge Modelling*, Singapore, A.A. Balkema, Rotterdam, The Netherlands, September 1994.
8. Lambe, P. C., and R. V. Whitman. Scaling for Earthquake Shaking Tests on a Centrifuge. *Proc., Soil Dynamics and Earthquake Engineering Conference*, Southampton, U.K., Vol. 1, 1982, pp. 367-378.
9. Hardin, B. O. Stress-Strain Behaviour. *Earthquake Engineering and Soil Dynamics. Proc., ASCE Geotechnical Engineering Division Special Conference*, Pasadena, Calif., 1978.
10. Duncan, J. M., and C. Y. Chang. Non-linear Analysis of Stress and Strain in Soils. *Journal of Soil Mechanics and Foundations Division, Proc., ASCE*, Vol. 96, 1970, pp. 1629-1653.

11. Taylor, D. W. *Fundamentals of Soil Mechanics*. John Wiley & Sons, New York, 1948.
12. Schofield, A. N, and C. P. Wroth. *Critical State Soil Mechanics*. McGraw-Hill, London, 1968.
13. Matsuoka, H., and T. Nakai. Stress-Strain Relationship of Soil Based on S.M.P. *Proc., 9th International Conference on Soil Mechanics and Foundation Engineering*, 1977, pp. 153-162.
14. Cundall, P. A. *FLAC User's Manual*. ITASCA Consulting Group, Inc. Minneapolis, Minn., 1993.

Publication of this paper sponsored by Committee on Modelling Techniques in Geomechanics.